Spatial and Seasonal Variations of Submesoscale Eddies in the Eastern Tropical Pacific Ocean

SHENGPENG WANG AND ZHAO JING

Physical Oceanography Laboratory/Collaborative Innovation Center of Marine Science and Technology, Ocean University of China, and Qingdao National Laboratory for Marine Science and Technology, Qingdao, China

HAILONG LIU

State Key Laboratory of Numerical Modeling for Atmospheric Sciences and Geophysical Fluid Dynamics, Institute of Atmospheric Physics, Chinese Academy of Sciences, Beijing, China

LIXIN WU

Physical Oceanography Laboratory/Collaborative Innovation Center of Marine Science and Technology, Ocean University of China, and Qingdao National Laboratory for Marine Science and Technology, Qingdao, China

(Manuscript received 5 April 2017, in final form 14 November 2017)

ABSTRACT

The spatial and seasonal variations of submesoscale eddy activities in the eastern tropical Pacific Ocean (2°–12°N, 95°–165°W) are investigated based on a 1/10° ocean general circulation model (OGCM). In the studied region, it is found that motions shorter than 500 km are subject to submesoscale dynamics with an $O(1)$ Rossby number and Richardson number and a −2 spectral slope for kinetic energy, suggesting that submesoscale eddies there can be well resolved by the model. Enhanced submesoscale eddy kinetic energy (SMKE) is found in the surface mixed layer centered at 5°N. A complete SMKE budget analysis suggests that the submesoscale eddies in the surface mixed layer are generated mainly by the barotropic instability and secondarily by the baroclinic instability. The nonlinear interactions lead to a significant forward energy cascade in the submesoscale range and play an important role in balancing the energy budget. As a response to the change of energy input through barotropic instability, the SMKE exhibits a pronounced seasonal cycle with the largest and smallest values occurring in boreal autumn and spring. Furthermore, the strong seasonal cycle plays an important role in modulating the seasonality of mixed layer depth (MLD). In particular, the restratification induced by the strong submesoscale eddies between July and October makes important contribution to the shoaling of MLD in this season.

1. Introduction

Submesoscale eddies, defined as flows with an $O(1)$ Rossby number and Richardson number (Thomas et al. 2008), are a ubiquitous feature in the upper ocean, as evidenced by the observation of the sun-glint photographs from space shuttles (Scully-Power 1986; Munk et al. 2000). They are strongly ageostrophic (Klein et al. 2008, 2011) and potentially make significant contribution to the downscale energy cascade (also known as the forward energy cascade) and energy dissipation (Capet et al. 2008c; Molemaker et al. 2010; Marchesiello et al. 2011; Barkan et al. 2015; Brüggemann and Eden 2015). Furthermore, they can produce strong vertical motions and thus have an impact on the nutrient supply and biogeochemistry of the upper ocean (Mahadevan and Archer 2000; Lévy et al. 2001, 2012; Rosso et al. 2014). Another important role of the submesoscale eddies in ocean dynamics is their influence on the upper-ocean stratification by limiting the deepening of the mixed layer (Nurser and Zhang 2000; Boccaletti et al. 2007; Fox-Kemper and Ferrari 2008; Brannigan et al. 2015; Couvelard et al. 2015).

Over the past two decades, a lot of effort has been put to understand the generation, propagation, and dissipation

Corresponding author: Zhao Jing, jingzhao198763@sina.com

DOI: 10.1175/JPO-D-17-0070.1

of the submesoscale eddies based on idealized, baroclinic, channel models and high-resolution regional models with realistic coastline and bottom topography (Capet et al. 2008a,b,c,d; Thomas et al. 2008; Klein et al. 2008; Lévy et al. 2010; Klein et al. 2011; Marchesiello et al. 2011; Haney et al. 2012; Ponte et al. 2013; Mensa et al. 2013; Sasaki et al. 2014). At midlatitudes, the submesoscale eddies are characterized by a horizontal scale of O(0.1–10) km. They are mainly furnished by the background available potential energy stored in the surface mixed layer through mixed layer instabilities, frontogenesis, and turbulent thermal winds (McWilliams 2016). In all these mechanisms, the energy conversion scales with the mixed layer depth (MLD) so that the seasonal variation of submesoscale eddy activity is strongly modulated by that of MLD. For instance, realistic high-resolution regional modeling studies show a net increase of submesoscale eddy activity in fall and winter when the MLD is deepest in the North Pacific Ocean (Sasaki et al. 2014). Observations also confirm that the submesoscale eddies become much stronger in winter than in summer along the Kuroshio, subtropical countercurrent bands, and the Gulf Stream when the MLD is deepest because of the atmospheric forcing (Callies et al. 2015; Qiu et al. 2017). Moreover, the submesoscale eddies can in turn reduce the MLD through the restratification process and thus exert a negative feedback on the development of seasonal cycle of MLD, as revealed in the high-resolution idealized numerical study by Couvelard et al. (2015).

So far the analyses on the submesoscale eddies are mainly confined to the midlatitude ocean with the submesoscale dynamics in the equatorial region still poorly assessed. It should be noted that the insights gained from the studies on submesoscale eddies at midlatitudes are not entirely applicable in the equatorial region because of the pronounced difference in the dynamical conditions between the midlatitudes and equatorial region. First, the mixed layer Rossby deformation radius in the equatorial region is much larger than that at the midlatitudes because of the reduced Coriolis parameter. Indeed, using a 3-month regional simulation, Marchesiello et al. (2011) finds that submesoscale eddies in the equatorial region have a horizontal scale more than an order of magnitude larger than that at midlatitudes, suggesting that they can be well resolved using a 1/10° ocean general circulation model (OGCM). Furthermore, the equatorial region has a complex flow system so that the strong strain induced by background flow may play an important role in generating the submesoscale eddies. In this case, the seasonal cycle of submesoscale eddies does not necessarily follow that of MLD, as at the midlatitudes (Callies et al. 2015; Qiu et al. 2017).

In this study, we analyze submesoscale eddies in the tropical Pacific Ocean based on a 1/10° realistic ocean simulation. In specific, we attempt to address the following problems: 1) the spatial and seasonal variations of submesoscale eddies, 2) the underlying dynamics responsible for the seasonal cycle of submesoscale eddies, and 3) the impact of submesoscale eddies on the seasonal cycle of MLD. The paper is organized as follows: Section 2 briefly describes the OGCM data and diagnostic framework in this study. Results are presented in section 3. Discussion is provided in section 4 followed by conclusions in section 5.

2. Data and methodology

a. Data

To explore the submesoscale eddies in the tropical Pacific Ocean, one of the hindcast runs of the State Key Laboratory of Numerical Modeling for Atmospheric Sciences and Geophysical Fluid Dynamics/Institute of Atmospheric Physics (LASG/IAP) Climate Ocean Model 2.0 (LICOM; Yu et al. 2012; Liu et al. 2014) is used in this study. The global model domain extends from 66°N to 79°S and from 180°W to 180°E, with a horizontal resolution of 1/10°. There are 55 levels in the vertical direction. In the upper 100 m, the thickness increases from 2.5 m near the surface to 8 m near 100 m. The model topography is constructed from the Digital Bathymetric Database 5 min compiled by the U.S. Navy Oceanographic Office. The scale-selective biharmonic horizontal viscosity and diffusivity schemes are used for momenta and tracers (temperature and salinity), respectively. Besides, a modified Richardson number–based scheme is adopted for the vertical mixing (Canuto et al. 2001, 2002). The lateral boundary conditions of this model are no-normal flow and no-slip conditions, while a quadratic bottom stress is applied with a drag coefficient of 2.6×10^{-3}. This eddy-resolving OGCM is first spun up for 12 years from Ocean Model International Cooperation Program (OMIP; Roske 2001), which is derived from the reanalysis product of the 15-yr European Centre for Medium-Range Weather Forecasts (ECMWF) Re-Analysis (ERA-15; Gibson et al. 1999). After this spinup integration, a 60-yr (1948–2007) hindcast integration is performed under daily mean atmospheric forcing from Co-ordinated Ocean–Ice Reference Experiments (CORE), version 2 (Large and Yeager 2004). This hindcast run shows good skills in the tropical Pacific Ocean. Specifically, the simulated cold tongue, Equatorial Undercurrent (EUC), South Equatorial Current (SEC), and tropical instability waves (TIWs) agree reasonably well with the observations (Fig. 1). The wave period of the modeled TIWs is in the range 15–40 days, which is consistent with the observation of Tropical Atmosphere Ocean (TAO) moorings (Fig. 1c). Moreover, the EUC at 140°W also compares well with the

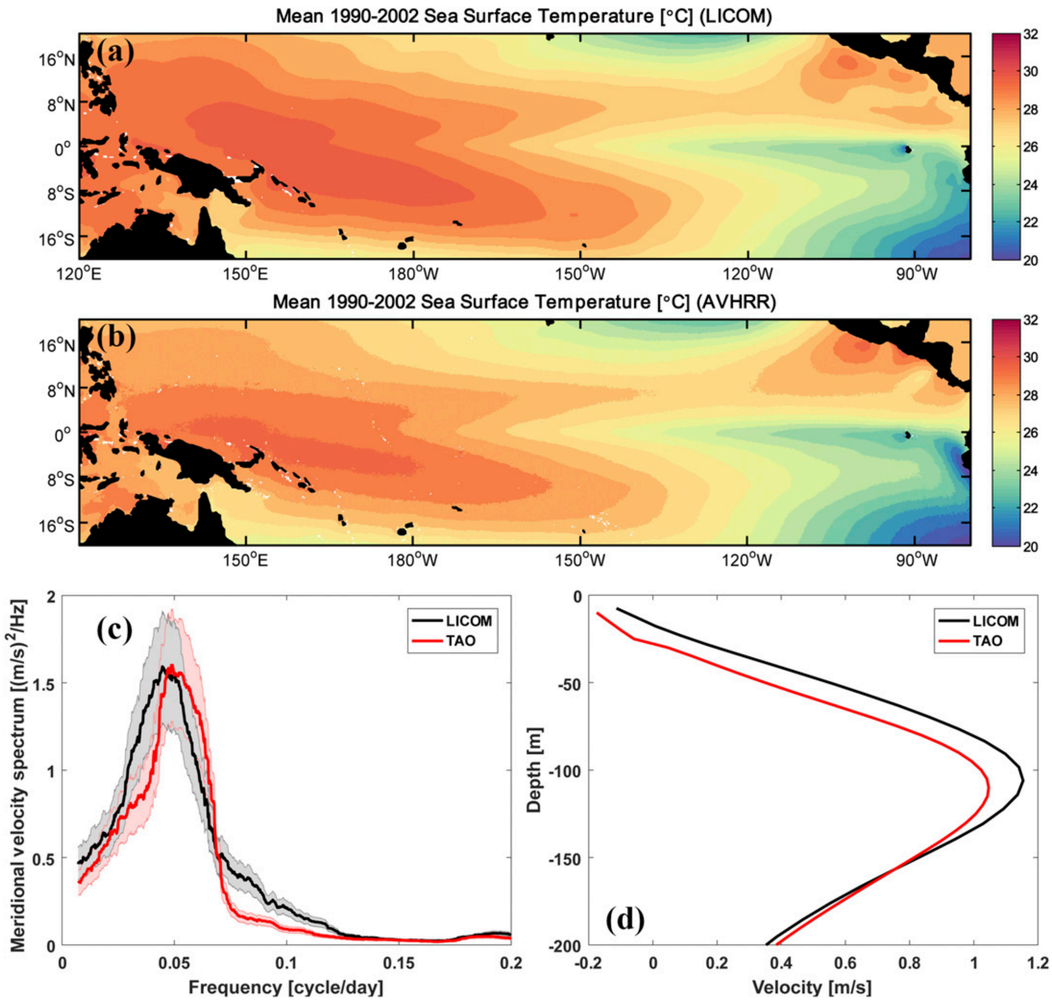

FIG. 1. Mean sea surface temperature (SST) derived from (a) LICOM and (b) AVHRR averaged from 1990 to 2002. (c) Frequency spectra of surface meridional velocity from LICOM and TAO mooring data at the 0°, 140°W. The shading error bar represents the 95% confidence interval. (d) Mean zonal velocity from LICOM and TAO mooring data at the 0°, 140°W. The data used here are from 1990 to 2007.

TAO moorings despite the slightly stronger magnitude (Fig. 1d). The bias might result from the uncertainties of the wind forcing in the model (Cravatte and Menkes 2009). In this study, the daily data from 1 January 1990 to 31 December 2007 are used to analyze the submesoscale eddies in the tropical Pacific Ocean with the modified topography in Luzon Strait for better description of the Kuroshio intrusion (Huang et al. 2017). It should be noted that the equator is a singular point for the Rossby number so that the dynamical definition for submesoscale flows does not apply (Thomas et al. 2008). Thus, we exclude the region within 2° of equator in the following analysis.

b. Submesoscale kinetic energy budget analysis

The governing equations for incompressible, Boussinesq, and hydrostatic flows can be expressed in a general form:

$$\frac{\partial u}{\partial t} + u\frac{\partial u}{\partial x} + v\frac{\partial u}{\partial y} + w\frac{\partial u}{\partial z} - fv = -\frac{1}{\rho_0}\frac{\partial}{\partial x}p + D_u, \quad (1)$$

$$\frac{\partial v}{\partial t} + u\frac{\partial v}{\partial x} + v\frac{\partial v}{\partial y} + w\frac{\partial v}{\partial z} + fu = -\frac{1}{\rho_0}\frac{\partial}{\partial y}p + D_v, \quad (2)$$

$$\frac{\partial p}{\partial z} = -\rho g, \quad \text{and} \quad (3)$$

$$\frac{\partial u}{\partial x} + \frac{\partial v}{\partial y} + \frac{\partial w}{\partial z} = 0, \quad (4)$$

where (u, v, w) is the 3D velocity, f is the Coriolis parameter varying with latitude, D_u and D_v represent the mixing terms for zonal and meridional velocities, p is the hydrostatic pressure, ρ is the density, and ρ_0 is the reference density chosen to be $1027.5\,\mathrm{kg\,m^{-3}}$.

We perform a Reynolds decomposition of the 3D flow field into background and submesoscale perturbations: $\mathbf{u} = \mathbf{u}' + \overline{\mathbf{u}}$, where the prime and overbar denote the submesoscale perturbations and background motions, respectively. In this study, the submesoscale perturbations are isolated by first high-pass filtering in the time domain and then high-pass filtering in the spatial domain. The high-pass filter in the time and spatial domains is defined as the residue of a temporal running mean over 5 days and a horizontal running mean over a 300 km × 300 km square, respectively. Therefore, the submesoscale eddies defined in this study consist of motions smaller than ~600 km and at the same time shorter than ~10 days. The rationale of using a high-pass filter in the time domain is to remove the contamination by small-scale, low-frequency motions that are unlikely to be subject to submesoscale dynamics. Previous studies (Eady 1949; Callies et al. 2015) suggest that the time scale of submesoscale eddies generated through mixed layer instability can be estimated as $N/(\Lambda f)$, where N is the background buoyancy, and $\Lambda = \sqrt{\overline{u}_z^2 + \overline{v}_z^2}$ is the vertical shear of background flow. Based on the LICOM simulation, it is found that the time scale of submesoscale eddies in the east equatorial Pacific is generally shorter than 10 days (not shown). Finally, it should be noted that there is no clear scale separation between submesoscale and large-scale background flows, and the definition of submesoscales in this study is heuristic. Nevertheless, as shown in the section 3a, the characteristics of defined submesoscale flows are generally consistent with submesoscale dynamics, lending supports to the validity of our definition.

The kinetic energy budget for submesoscale perturbations is expressed as

$$\frac{\partial}{\partial t}\mathrm{SMKE} = -\underbrace{\left\langle \nabla\cdot\left[\mathbf{u}\frac{1}{2}\rho_0(u'^2+v'^2)\right]\right\rangle}_{\mathrm{AKE}} - \underbrace{\langle\nabla\cdot(\mathbf{u}'p')\rangle}_{\mathrm{PKE}} - \underbrace{\langle g\rho'w'\rangle}_{\mathrm{IKE}} - \underbrace{\langle\rho_0(u'\mathbf{u}\cdot\nabla\overline{u}+v'\mathbf{u}\cdot\nabla\overline{v})\rangle}_{\mathrm{MKE}}$$
$$+\underbrace{\langle\rho_0(u'D_u+v'D_v)\rangle}_{\mathrm{DKE}} - \underbrace{\left\langle\left[\rho_0\left(u'\frac{\partial\overline{u}}{\partial t}+v'\frac{\partial\overline{v}}{\partial t}\right)+\nabla\cdot(\mathbf{u}'\overline{p})+g\overline{\rho}w'\right]\right\rangle}_{\mathrm{TRP}}, \quad (5)$$

where $\mathrm{SMKE} = \langle(1/2)\rho_0(u'^2+v'^2)\rangle$ is the kinetic energy of submesoscale perturbations, < > denotes the temporal average between 1990 and 2007, and $\nabla\cdot$ is the divergence operator. AKE and PKE represent the redistribution of submesoscale eddy kinetic energy (SMKE) through advection and pressure work, respectively. IKE is the conversion of available potential energy of submesoscale perturbations to SMKE. MKE represents the energy exchange between submesoscale perturbations and background flow through barotropic instability. DKE denotes the change of SMKE associated with the viscosity effect (e.g., interior dissipation and surface wind power) and is computed as the residue of the energy budget equation. The emergence of TRP is due to the nonorthogonality between $\mathbf{u}'$ and $\overline{\mathbf{u}}$ and has no clear dynamical interpretation. However, it is found that the TRP term is an order of magnitude smaller than the MKE and IKE terms. In the following analysis, we will drop the TRP term, in which case Eq. (5) is reduced to the standard eddy kinetic energy equation.

Because of the nonlinear interaction, motions of different scales can interact with each other, leading to an energy exchange among different scales. Therefore, it is useful to analyze the kinetic energy budget of submesoscale motions in the spectral domain (referred to as the spectral SMKE budget henceforth). Different from the calculation of submesoscale kinetic energy budget in the physical space, here the perturbations (primed quantities) are computed by only using a high-pass filter in the time domain as the motions at different spatial scales are automatically distinguished in the spectral analyses. The spectral SMKE budget is

$$\partial_t \mathrm{SMKE}_K = \mathrm{PKE}_K + \mathrm{IKE}_K + \mathrm{AKE}_K + \mathrm{MKE}_K + \mathrm{DKE}_K, \quad (6)$$

$$\mathrm{SMKE}_K = \Re\left[0.5\widehat{\mathbf{u}'_h}^* \cdot \widehat{\mathbf{u}'_h}\right], \quad (7)$$

$$\mathrm{PKE}_K = \Re\left[-\widehat{\mathbf{u}'_h}^* \cdot \widehat{\frac{1}{\rho_0}\nabla p'}\right], \quad (8)$$

$$\mathrm{IKE}_K = \Re\left[-\frac{g}{\rho_0}\widehat{w'}^* \cdot \widehat{\rho'}\right], \quad (9)$$

$$\mathrm{AKE}_K = \mathrm{A}_H + \mathrm{A}_V = \Re\left[-\widehat{\mathbf{u}'_h}^* \cdot \widehat{(\mathbf{u}'_h\cdot\nabla_h)\mathbf{u}'_h} - \widehat{\mathbf{u}'_h}^* \cdot \widehat{w'\frac{\partial\mathbf{u}'_h}{\partial z}}\right], \quad (10)$$

$$\mathrm{MKE}_K = \Re\left[-\widehat{\mathbf{u}'_h}^* \cdot \widehat{(\overline{\mathbf{u}}\cdot\nabla)\mathbf{u}'_h} - \widehat{\mathbf{u}'_h}^* \cdot \widehat{(\mathbf{u}'\cdot\nabla)\overline{\mathbf{u}}_h} - \widehat{\mathbf{u}'_h}^* \cdot \widehat{(\overline{\mathbf{u}}\cdot\nabla)\overline{\mathbf{u}}_h}\right], \quad \text{and} \quad (11)$$

$$\mathrm{DKE}_K = \mathrm{D}_H + \mathrm{D}_V = \Re\left[\widehat{\mathbf{u}'_h}^* \cdot \widehat{D'}\right], \quad (12)$$

where $\hat{}$ denotes the two-dimensional Fourier transform, ∇_h is the horizontal divergence operator, * is the complex conjugate, and $\Re$ is the real part operator. SMKE_K is the power spectral density of kinetic energy of submesoscale perturbations where the subscript K denotes the magnitude of wave vector (k_x, k_y). The terms PKE_K, IKE_K, AKE_K, MKE_K, and DKE_K are the counterparts of PKE, IKE, AKE, MKE, and DKE in the spectral space. Equation (6) is analogous to the spectral kinetic energy budget derived by Capet et al. (2008d) except the term MKE_K. This is because Capet et al. (2008d) analyze the kinetic energy budget of total flow so that there is no energy transfer through barotropic instability. To evaluate the individual terms in Eq. (6), we perform a 2D discrete Fourier transform to u', v', and individual terms in Eqs. (1) and (2) after removing their areal mean value. To reduce the Gibbs phenomena, a 2D window function composed of nine half-overlapping Hanning windows in each spatial direction is applied before the 2D FFT (Arbic et al. 2013). It should be noted that such a window function makes the velocity along the lateral boundaries become zero, artificially suppressing the advection of SMKE into or out of the domain. Nevertheless, as demonstrated in section 3 (see Fig. 6), the advection effect plays a negligible role compared to other terms in the SMKE budget. In this case, the term AKE_K in Eq. (6) is mainly contributed by the energy exchange among different wavenumbers. It redistributes the kinetic energy in the wavenumber space without affecting the total SMKE. Another deficiency of using the window function is the weakening of signal variability. This tends to underestimate the magnitude of individual terms in the spectral SMKE budget. Nevertheless, these biases are tolerable for our qualitative analysis.

Finally, the kinetic energy spectral flux is calculated following Capet et al. (2008d) and Marchesiello et al. (2011) by integrating the AKE_K term with respect to K and assuming that the flux vanishes at the highest wavenumber $K_{\max}$:

$$\Pi(k) = \int_K^{K_{\max}} \mathrm{AKE}_K \, dK. \tag{13}$$

It should be noted that there exist alternative methods for the calculation of the kinetic energy spectral flux from observations and numerical simulations (Scott and Wang 2005; Schlösser and Eden 2007; Ni et al. 2014). However, the method adopted in this study is built on the spectral SMKE budget equation and is thus readily applied. Furthermore, the main result is found insensitive to the adopted computational methods.

3. Results

a. Spatial and seasonal variations of submesoscale eddies in the tropical Pacific Ocean

The surface SMKE in the equatorial Pacific Ocean exhibits pronounced spatial variability (Fig. 2a). The submesoscale eddy activity is significantly stronger in the eastern Pacific than in the western Pacific with a strong peak at the latitude band 4°–8°N. This peak resides in the region where the background flow exhibits strong horizontal strain rate $S = \sqrt{(\overline{u}_x - \overline{v}_y)^2 + (\overline{u}_y + \overline{v}_x)^2}$ (Fig. 2b), suggesting that the barotropic instability may play an important role in the generation of submesoscale eddies. Furthermore, it is coincident with the strong temperature front along the northern edge of TIWs (Figs. 2c,d), so that the baroclinic instability may be also important in generating the submesoscale eddies. In the following analysis, we will focus on the region 2°–12°N, 95°–165°W, as it has the strongest submesoscale eddy activity (SSA region henceforth).

Figure 3 displays the wavenumber spectrum of total surface kinetic energy in the SSA region. The spectral level remains relatively flat from the largest resolved spatial scale (~8000 km) to ~800 km and then decreases rapidly as the spatial scale is further reduced. In particular, the spectrum is characterized by a k^{-2} power law within 80–500 km. As the spatial scale further reduces, the spectral slope becomes progressively steeper, implying the significant influence of numerical dissipation on these scales. We remark that a k^{-2} power law between 80 and 500 km is distinguished from a k^{-3} power law derived from the interior quasigeostrophic turbulence theory (Charney 1971) but is consistent with the prediction from mixed layer instabilities (Fox-Kemper et al. 2008). This provides strong evidence that the perturbations defined in this study are subject to submesoscale dynamics. Indeed, the Rossby number and Richardson number of perturbation flows are generally of $O(1)$ in the SSA region (Figs. 2e,f), lending further support to our argument. Similar to the situation at midlatitudes (e.g., Capet et al. 2008a; Thomas et al. 2008; Klein et al. 2008; McWilliams 2016), the SMKE in the SSA region is mainly confined to the surface mixed layer [Fig. 4a; MLD is defined at the depth where the temperature is 0.3°C lower than the surface value following Menkes et al. (2006)]. The averaged SMKE from 1990 to 2007 in the surface mixed layer is about 12 J m^{-3} and decreases to 5 and 2 J m^{-3} at 100 and 150 m, respectively. In addition to the SMKE, the spectral slope between 80 and 500 km also varies significantly with depth (Fig. 4b). It becomes steeper as the depth increases. At 150 m, the slope is close to k^{-3}, implying that

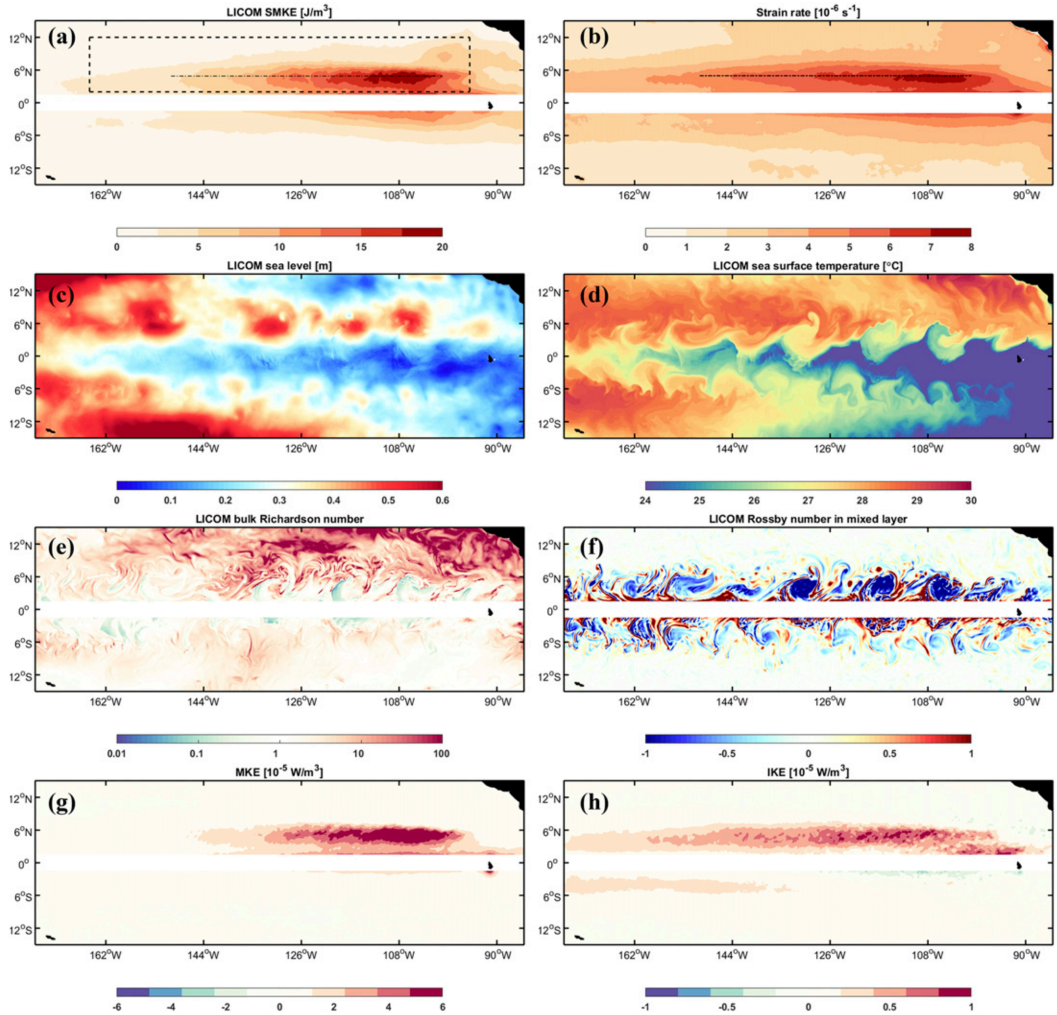

FIG. 2. (a) Spatial distribution of SMKE averaged from 1990 to 2007 based on LICOM. Snapshots of (c) SSH, (d) SST, (e) bulk Richardson number in mixed layer, and (f) Rossby number in mixed layer on 1 Oct 1998. Spatial distribution of temporal mean (b) strain rate, (g) MKE, and (h) IKE averaged over the upper 50 m. The dashed box in (a) denotes the SSA region and the dashed line represents 5°N.

the perturbed flows in the thermocline are nearly quasigeostrophic.

Figure 5a displays the seasonal cycle of the mixed layer SMKE zonally averaged in the SSA region. For the regional-mean value, the peak-to-peak SMKE difference accounts for 53% of the annual-mean SMKE level. The phase is generally coherent in the SSA region. At all the latitudes, the maximum and minimum occur in the September–October and April–May, respectively. The amplitude of the seasonal cycle varies strongly with the latitude, and it becomes insignificant north of 7°N. Furthermore, the spectral slope between 80 and 500 km also exhibits an evident seasonal cycle with its phase similar to that of SMKE (Fig. 5b). Within 0–150 m, the slope is shallowest in November and steepest in April.

b. *Energy budget analysis*

To explore the underlying mechanisms modulating the seasonal cycle of SMKE, we examine the SMKE budget in the steady state and its seasonal variations in the SSA region.

1) STEADY STATE

Figure 6 displays the temporally and zonally averaged SMKE budget in the SSA region. The MKE term plays a dominant role in generating the submesoscale eddies, accounting for about 78% of SMKE production in the upper 50 m (the mean MLD in the SSA region). It peaks at the surface and is concentrated between 2° and 7°N (Fig. 2g), coincident with the strong horizontal strain rate of the background flow (Fig. 2b). The IKE term acts

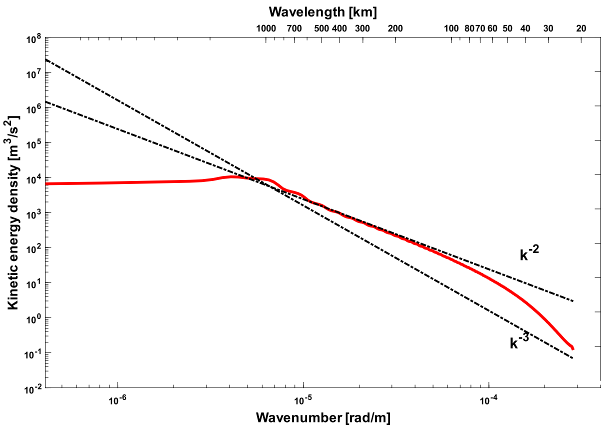

FIG. 3. Wavenumber spectrum of total surface horizontal velocity in the SSA region derived from LICOM. The black lines indicate −2 and −3 spectrum slopes.

as a secondary but nonnegligible energy source for submesoscale eddies, contributing to about 14% of SMKE production. It reaches its maximum just above the base of mixed layer between 3° and 6°N, where the TIWs produce a strong temperature front and favor the occurrence of mixed layer instability (Figs. 2d,h). This suggests the important role of TIWs in energizing the submesoscale eddies. The AKE term is characterized by a dipole structure with large negative values near the sea surface between 2° and 5°N and large positive values near the base of mixed layer between 4° and 7°N. Its value integrated in the upper 50 m in the SSA region is close to zero (less than 10% of SMKE production in the mixed layer), indicating that the advection acts to redistribute the SMKE in the mixed layer with no significant contribution to the total SMKE. The PKE also exhibits a dipole structure. However, its positive peak is located well below the mixed layer. Therefore, the PKE term radiates the SMKE generated in the mixed layer downward into the thermocline, accounting for 34% of SMKE sink in the mixed layer. The DKE is negative throughout the SSA region and is responsible for the remaining 66% of SMKE sink in the mixed layer.

Consistent with the energy budget in the physical space, the spectral energy budget in the submesoscale range (80–500 km) also indicates that the barotropic and baroclinic instabilities are the dominant energy sources for SMKE in the mixed layer, with the sink of SMKE mainly through the pressure work and mixing processes (Fig. 7a). In addition, the spectral energy budget clearly reveals a mismatch of wavenumber for energy source and sink. On one hand, the MKE_K generally decreases with increasing wavenumbers while the IKE_K peaks around 144 km, leading to less than 20% of the energy injected at wavelength shorter than 100 km. The wavelength with the strongest baroclinic instability is comparable to the mixed layer deformation radius (22.9 km) multiplied by a factor of 2π near 5°N (Boccaletti et al. 2007), implying that the mixed layer instability makes dominant contribution to the $\mathrm{IKE_K}$. On the other hand, the energy loss through DKE_K is most dominant around 100 km. Correspondingly, about 40% of the energy sink occurs below 100 km. To maintain an equilibrium state, energy has to be transferred downscales. This is confirmed by the dipolar structure of AKE_K and the positive definite spectral energy flux Π in the wavenumber space (Fig. 8a). In other words, nonlinear interactions lead to the forward energy cascade in the submesoscale range and play an important role in balancing the energy budget.

2) SEASONAL VARIATIONS

Figure 9 displays the differences of SMKE budget terms between June and September and January and April. The former and latter correspond to the period with the growing and decaying submesoscale eddy activity

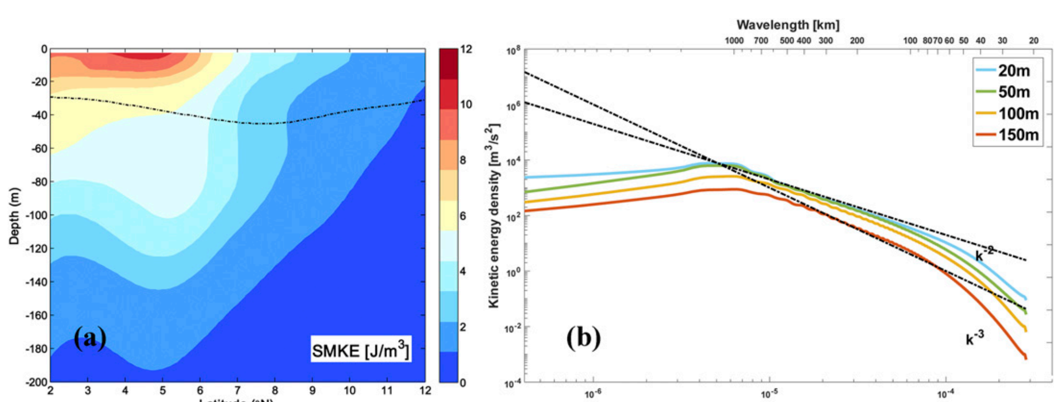

FIG. 4. (a) Latitude–depth plot of SMKE zonally averaged over 95°–165°W. The black dotted–dashed line represents the zonally averaged MLD. (b) Wavenumber spectrum of total horizontal velocity in the SSA region at various depths. The black lines indicate −2 and −3 spectrum slopes.

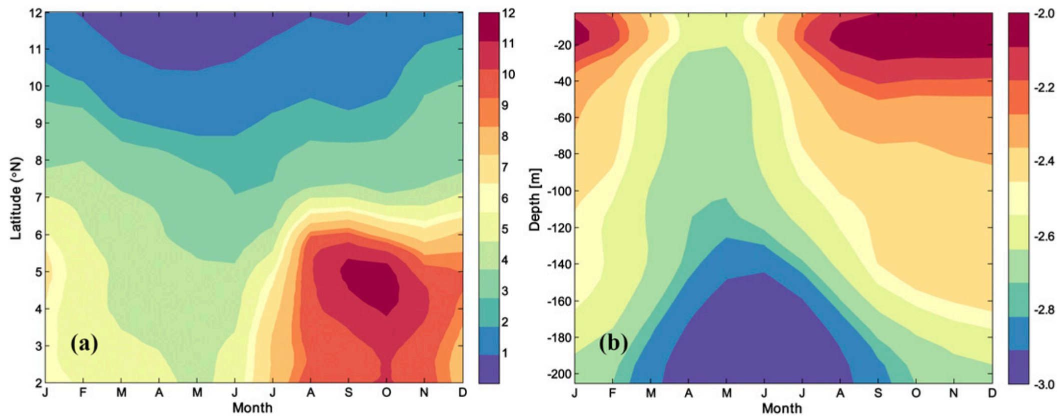

FIG. 5. (a) Monthly mean SMKE ($J\,m^{-3}$) zonally averaged over 95°–165°W and vertically averaged in the upper 50 m. (b) Monthly mean SMKE spectral slope over 80–500 km in the SSA region.

in the SSA region, respectively (Fig. 5a). The total energy production of SMKE (MKE + IKE) in the growing phase is about 3 times the value in the decaying phase. The increased energy production in the growing phase is largely balanced by the enhanced dissipation through the DKE term and downward radiation of SMKE into the thermocline through the PKE term. The remaining portion contributes to a positive SMKE tendency term, resulting in growing submesoscale eddy activity.

The enhanced energy production in the growing phase is mainly attributed to the change of MKE term that accounts for more than 75% of the energy production increase. The IKE term plays a secondary and contributes less than 19% of the energy production increase. Therefore, we conclude that the seasonal cycle of SMKE in the SSA region is mainly controlled by the strength of barotropic energy conversion. This is distinguished from the scenario at the midlatitudes where the baroclinic

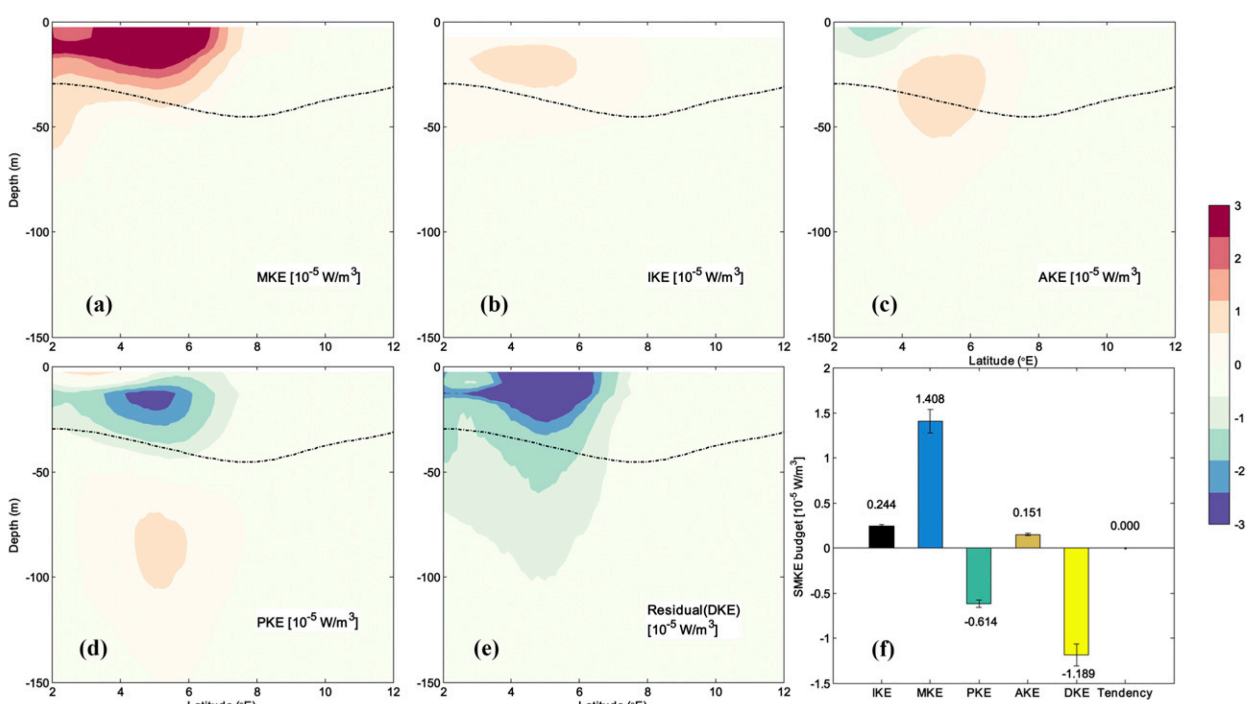

FIG. 6. Latitude–depth plots of (a) MKE, (b) IKE, (c) AKE, (d) PKE, and (e) DKE zonally averaged over 95°–165°W. The black dotted–dashed line denotes the zonally averaged MLD. (f) SMKE budget terms averaged in the upper 50 m of SSA region. The error bar represents the standard error.

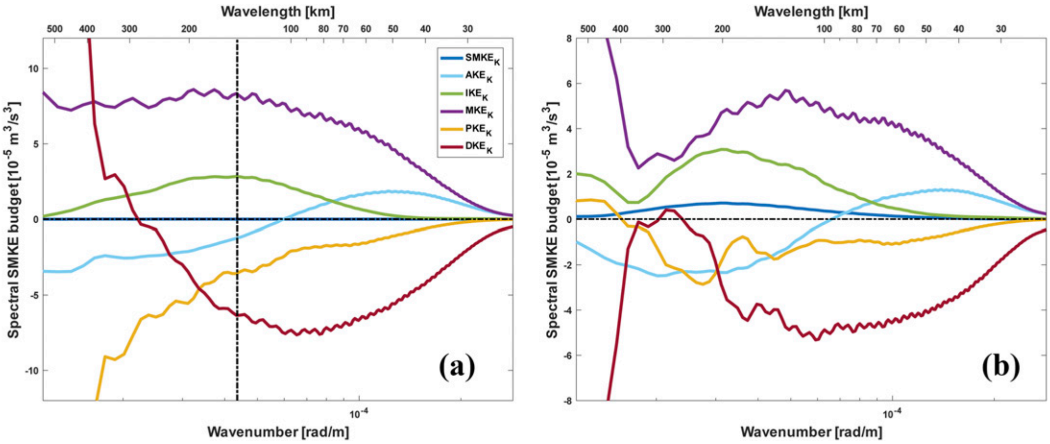

FIG. 7. (a) Spectral SMKE budget averaged in the upper 50 m of the SSA region. (b) As in (a), but for the difference between the decaying (January–April) and growing (June–September) periods of SMKE. The vertical dashed black line denotes the mixed layer deformation radius.

energy conversion plays a dominant role (e.g., Sasaki et al. 2014; Callies et al. 2015; Qiu et al. 2017).

Figure 7b displays the difference of the spectral energy budget averaged in the upper 50 m between the growing (June–September) and decaying (January–April) phases. It also suggests that the seasonal cycle of SMKE is mainly caused by the seasonal variations of energy input through barotropic instability and to a less extent baroclinic instability. Another notable feature is that the downscale energy cascade (positive Π) through the AKE$_K$ term is also enhanced in the growing phase compared to the decaying phase (Figs. 7b, 8b). This acts to slow down the growth of submesoscale eddy activity by transferring more energy to smaller scales where the energy tends to be more efficiently damped through physical or numerical dissipation. It thus implies that the downward energy cascade caused by the nonlinear interactions might play an important role in modulating the seasonal cycle of SMKE.

c. *Restratification by submesoscale eddies*

Existing studies reveal that the submesoscale eddies play a role in the upper-ocean heat budget (Boccaletti et al. 2007; Fox-Kemper and Ferrari 2008; Brannigan et al. 2015). In particular, they contribute to the restratification of surface mixed layer. However, it remains poorly understood how important the restratification induced by submesoscale eddies is compared to that induced by other processes. In the east equatorial Pacific, TIWs are suggested to play an important role in restratifying the

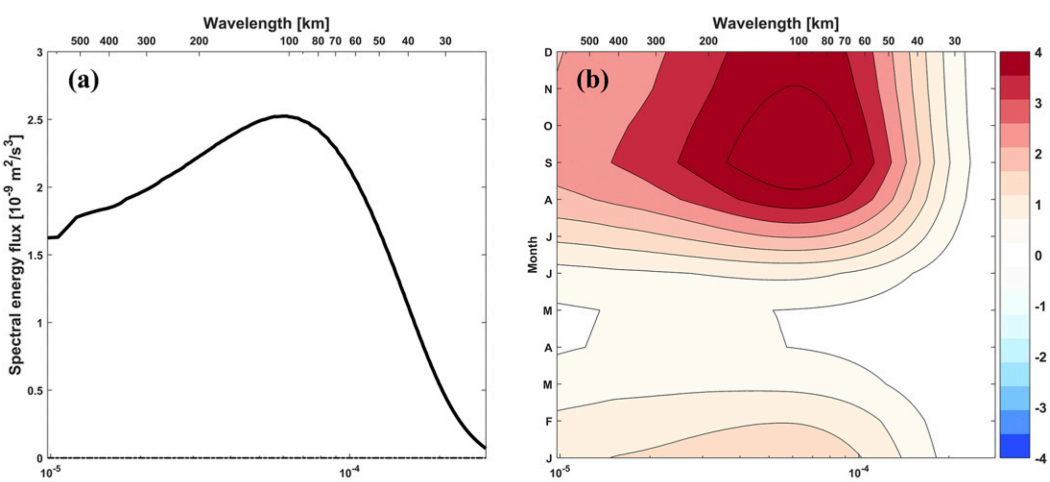

FIG. 8. (a) Spectral energy flux rate Π defined by Eq. (13) averaged in the upper 50 m of the SSA region and temporally from 1990 to 2007. (b) Seasonal cycle of the spectral energy flux rate Π ($\times 10^{-9}$ m^2 s^{-3}) averaged in the SSA region.

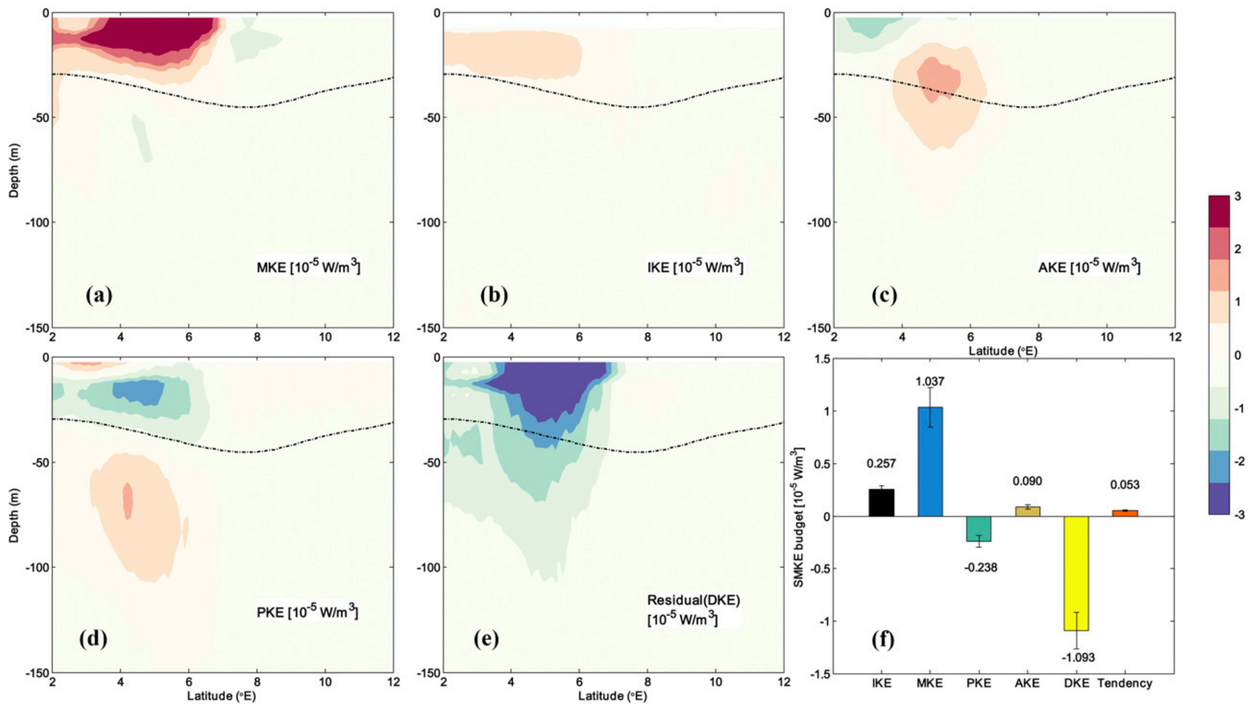

FIG. 9. As in Fig. 6, but for the difference between the decaying (January–April) and growing (June–September) periods of SMKE.

surface mixed layer (Menkes et al. 2006). In this section, we compare the relative importance between TIWs and submesoscale eddies to the heat budget. The variables are decomposed as follows:

$$X = \overline{X} + X', \tag{14}$$

where X is any variable, $\overline{X}$ represents the large-scale background, and X' represents the submesoscale eddy component defined in section 2b. The TIWs signals are further isolated from the large-scale background, that is, $\overline{X} = X_m + X_{\mathrm{tiw}}$, where X_{tiw} is the TIWs signal defined as the perturbations within the period 15–40 days (Lyman et al. 2007), and X_m is the remaining component mainly associated with the equatorial circulation. Then the time-mean temperature equation over 1990–2007 is given by

$$\begin{aligned}\langle \partial_t T\rangle = &-\underbrace{\langle \mathbf{U}_m \cdot \nabla T_m\rangle}_{A_m} - \underbrace{\langle \mathbf{U}_{\mathrm{tiw}} \cdot \nabla T_{\mathrm{tiw}}\rangle}_{A_{\mathrm{tiw}}} - \underbrace{\langle \mathbf{U}' \cdot \nabla T'\rangle}_{A_{\mathrm{sub}}} \\ &+ \underbrace{\langle (K_H T_x)_x + (K_H T_y)_y\rangle}_{D_l} + \underbrace{\langle (K_V T_z)_z + I(z)\rangle}_{D_v} \\ &+ \langle \mathrm{A}_{\mathrm{cross}}\rangle \approx 0,\end{aligned} \tag{15}$$

where K_H and K_V are the horizontal and vertical diffusion coefficients; A_m is the advection by the equatorial circulation; A_{tiw} is the advection by the TIWs; A_{sub} is the advection by the submesoscale eddies; A_{cross} is the cross term (e.g., $u_m \partial_x T_{\mathrm{tiw}}$) resulting from the non-orthogonality among X_m, X', and X_{tiw}; D_l is the horizontal diffusion; and D_v is the temperature change caused by the divergence of vertical turbulent and radiation heat fluxes. As the vertical diffusion coefficient is not available, D_v is computed as the residue of the temperature budget. It is found that the vertically integrated D_v agrees with $Q_{\mathrm{net}}/C_p\rho_0$ reasonably well (differing by less than 30% throughout 2°–12°N), where Q_{net} is the net surface heat flux and C_p is the heat capacity of seawater, giving us confidence on the validity of estimated D_v.

Figure 10 represents the individual terms in Eq. (15) zonally averaged over 95°–165°W. The terms A_m, A_{tiw}, A_{sub}, and D_v are the four dominant components in the heat budget with D_l and A_{cross} playing a negligible role. Consistent with previous studies (Menkes et al. 2006; Graham 2014), A_m is negative in the upper 100 m near the equator but has a dipole pattern between 3° and 6°N. The former is due to the import of cold water from the cold tongue, while the latter is due to the downwelling at 5°N. The term A_{tiw} leads to warming near the equator and cooling between 5°N and 8°N (Fig. 10b) because of the TIW-induced heat exchange between cold water on the equator and warm water off the equator (e.g., Baturin and Niiler 1997; Kennan and

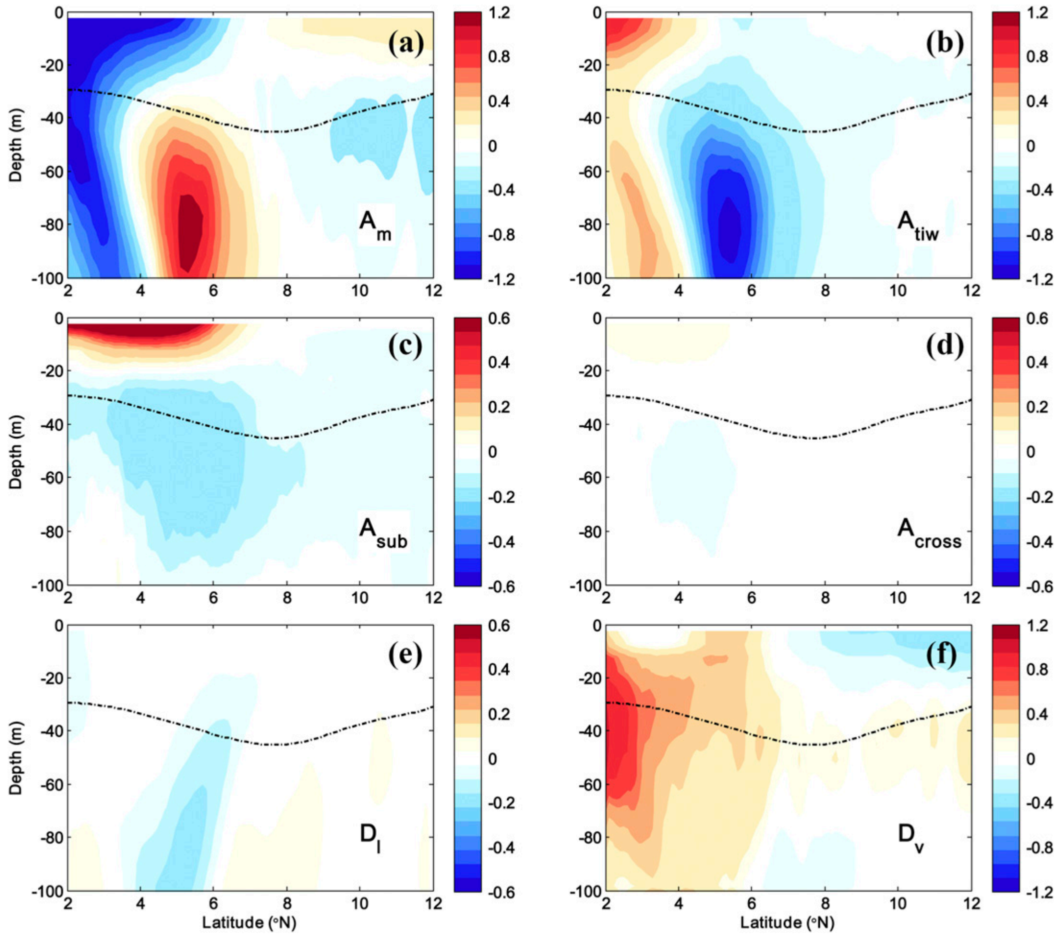

FIG. 10. The (a) A_m, (b) A_{tiw}, (c) A_{sub}, (d) A_{cross}, (e) D_l, and (f) D_v zonally averaged over 95°–165°W and temporally averaged from 1990 to 2007 (K month^{-1}). The black dotted–dashed lines denote the zonally averaged MLD.

Flament 2000; Menkes et al. 2006; Graham 2014). The term A_{sub} exhibits a dipole pattern between 3° and 6°N. It leads to warming in the mixed layer but cooling below the mixed layer, acting to restratify the upper ocean. The term D_v warms the upper ocean near the equator as a result of gaining heat flux from the atmosphere. To the north of 8°N, the downward heat flux into the ocean is close to zero and D_v acts to mix the water within and below the mixed layer, leading to cooling and warming within and below the mixed layer, respectively. Within 3°–6°N, A_m acts to deepen the mixed layer, whereas A_{tiw}, A_{sub}, and D_v tend to restratify the mixed layer. It should be noted that the restratification induced by A_{sub} is comparable to that by A_{tiw} and stronger than that by D_v, implying that the submesoscale eddies might play an important role in modulating the MLD.

To evaluate the modulation of seasonality of MLD by submesoscale eddies, we compute the seasonal cycle of MLD averaged within 3°–6°N, 95°–165°W, where the restratification process by submesoscale eddies is most significant. As shown in Fig. 11a, the regional mean MLD within 3°–6°N, 95°–165°W derived from the LICOM exhibits significant seasonal variations. The peak-to-peak MLD difference is 14 m. Although such an amplitude is much smaller than that at midlatitudes (Kara et al. 2003), it accounts for 30% of the annual-mean MLD level and is nonnegligible. Its phase is generally consistent with that derived from the Argo data, giving confidence on the reliability of LICOM in simulating the mixed layer dynamics. We remark that the phase of the seasonal cycle of MLD in this region is more complicated than that at the midlatitudes. Unlike the midlatitudes, it exhibits two shoaling processes. The primary shoaling occurs during January–April, while the secondary shoaling occurs during July–October. To explore the underlying reasons for these two shoaling processes, the

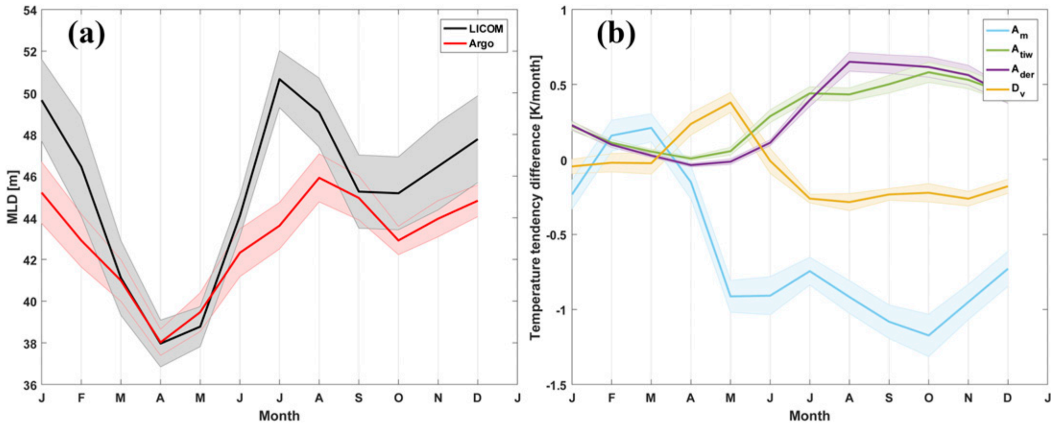

FIG. 11. The monthly average of (a) MLD and (b) ΔA_m, $\Delta A_{\rm tiw}$, $\Delta A_{\rm sub}$, and ΔD_v within 3°–6°N, 95°–165°W. The error bar represents the standard error.

difference of A_m, $A_{\rm tiw}$, $A_{\rm sub}$, and D_v within the mixed layer (0–35 m) and below the mixed layer (35–50 m) is computed and referred to as ΔA_m, $\Delta A_{\rm tiw}$, $\Delta A_{\rm sub}$, and ΔD_v. A positive difference corresponds to the restratification, whereas a negative difference corresponds to the destratification. Here, 35 m is the time-mean MLD, and the lower bound, that is, 50 m, is chosen somewhat arbitrarily. However, sensitivity tests suggest that changing the lower bound from 40 to 60 m does not have any substantial impact on the following results.

Figure 11b displays the seasonal cycles of ΔA_m, $\Delta A_{\rm tiw}$, $\Delta A_{\rm sub}$, and ΔD_v averaged within 3°–6°N, 95°–165°W. While the TIWs and submesoscale eddies act to restratify the mixed layer throughout the year, the mean flow and vertical mixing can either lead to restratification or destratification, depending on the seasons. During January–April, all four terms act to restratify the mixed layer, resulting in rapid reduction of MLD. During July–October, the mean flow and vertical mixing lead to almost the strongest destratification in the year and thus are not responsible for the shoaling of mixed layer in this season. This implies the reduced MLD during July–October might result from the restratification by TIWs and submesoscale eddies. Indeed, their restratification effects are significantly enhanced and both reach their maximum during this season, contributing to the shoaling of mixed layer.

4. Discussion

The above analysis indicates that the barotropic instability plays a dominant role in generating the submesoscale eddies in the SSA region. In this section, we make detailed analysis of the MKE term and attempt to reveal its origin.

We decompose the MKE term into six terms as

$$\mathrm{MKE}_1 = -\left\langle \rho_0 u'u \cdot \frac{\partial \overline{u}}{\partial x} \right\rangle, \tag{16}$$

$$\mathrm{MKE}_2 = -\left\langle \rho_0 v'v \cdot \frac{\partial \overline{v}}{\partial y} \right\rangle, \tag{17}$$

$$\mathrm{MKE}_3 = -\left\langle \rho_0 u'v \cdot \frac{\partial \overline{u}}{\partial y} \right\rangle, \tag{18}$$

$$\mathrm{MKE}_4 = -\left\langle \rho_0 v'u \cdot \frac{\partial \overline{v}}{\partial x} \right\rangle, \tag{19}$$

$$\mathrm{MKE}_5 = -\left\langle \rho_0 u'w \cdot \frac{\partial \overline{u}}{\partial z} \right\rangle, \quad \text{and} \tag{20}$$

$$\mathrm{MKE}_6 = -\left\langle \rho_0 v'w \cdot \frac{\partial \overline{v}}{\partial z} \right\rangle, \tag{21}$$

where the MKE_1 and MKE_2 represent the contribution of the horizontal normal strain to the MKE term, MKE_3 and MKE_4 are the contribution of horizontal shear strain, and MKE_5 and MKE_6 are the contribution of vertical shear. In the upper 50 m of SSA region, MKE_2 and MKE_6 make dominant contribution to the MKE, whereas the sum of remaining terms contributes to less than 10% and is thus negligible (Fig. 12a). This is distinct from the barotropic production for the mesoscale motions in this region, which is mainly attributed to the meridional shear of background zonal flow, that is, the MKE_3 term (Holmes and Thomas 2016).

As the North Equatorial Countercurrent (NECC) and SEC are zonally directed, they do not contribute to the MKE_2 and MKE_6 terms. It is likely that MKE_2 and MKE_6 might be mainly attributed to TIWs, given their energetic meridional current. To isolate the contribution of TIWs, we recompute the MKE_2 and MKE_6 terms by only retaining the components between 15 and

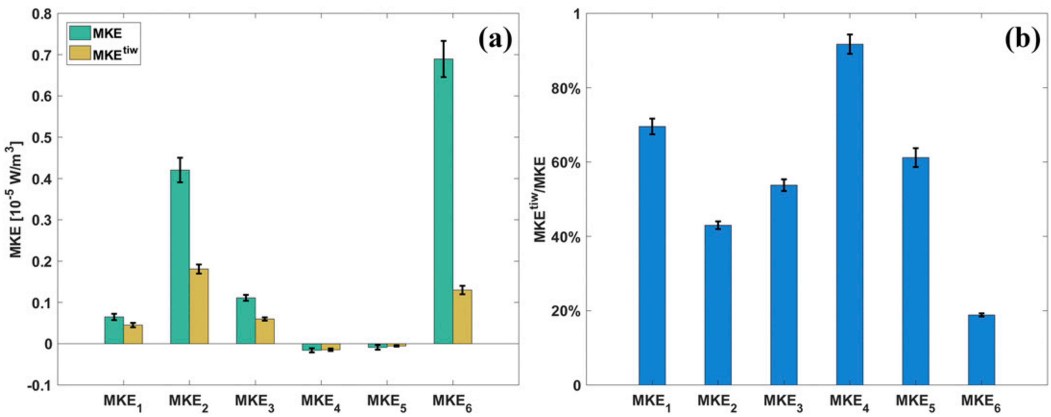

FIG. 12. (a) Decomposition of MKE (green) and MKE^{tiw} (yellow) terms averaged in the upper 50 m of the SSA region. (b) The contribution of TIWs to the individual terms of the total MKE. The error bar represents the standard error.

40 days in $\overline{u}$ and $\overline{v}$ (denoted as MKE_2^{tiw} and MKE_6^{tiw}). The value of MKE_2^{tiw} is about 43% of MKE_2 (Fig. 12b), confirming the important role of TIWs in MKE_2. However, the TIWs contribute to less than 19% of MKE_6 (Fig. 12b). Therefore, they are not responsible for the strong meridional vertical shear and associated kinetic energy transfer in the SSA region.

A possible candidate responsible for $d\overline{v}/dz$ in MKE_6 is the Ekman flow driven by surface wind stress. To test this hypothesis, we compute the vertical shear of Ekman flow. As the background density front could have an important influence on the vertical shear of Ekman flow, we adopt the frontal Ekman equation (Cronin and Kessler 2009) as

$$
\begin{aligned}
&if\mathbf{u}_a = \nu\frac{\partial^2\mathbf{u}_a}{\partial z^2} \\
&\frac{\partial \mathbf{u}_a}{\partial z} = \frac{1}{\rho_0\nu}\tau_0 - \frac{\partial \mathbf{u}_g}{\partial z}, \quad \text{at} \quad z = 0 \\
&\mathbf{u}_a = 0, \qquad\qquad\quad \text{at} \quad z \to -\infty,
\end{aligned}
\tag{22}
$$

where $\mathbf{u}_a$ is the ageostrophic Ekman flow, $\mathbf{u}_g$ is the geostrophic flow balanced with the density front, τ_0 is the surface wind stress, and ν is the vertical viscosity. As the exact value for ν is unknown, we treat it as a tuning parameter. It is found that the magnitude of time-mean $|\partial\overline{v}_a/\partial z|$ in the mixed layer decreases as the value of ν increases. However, for the value of ν within a reasonable range, that is, 10^{-3}–$10^{-2}\,m^2\,s^{-1}$ (Santiago-Mandujano and Firing 1990; Cronin and Kessler 2009), the magnitude of time-mean $|\partial\overline{v}_a/\partial z|$ in the mixed layer is much larger than that of $|\partial\overline{v}_g/\partial z|$ (Figs. 13a–c). In particular, when the value of ν is set as 8×10^{-3}, both the spatial distribution and magnitude of time-mean $|\partial\overline{v}_a/\partial z|$ in the mixed layer agree reasonably well with those of $|\partial\overline{v}/\partial z|$ (Figs. 13d,f). Furthermore, the time series of mean $|\partial\overline{v}_a/\partial z|$ averaged in the mixed layer of SSA region is tightly related to that of $|\partial\overline{v}/\partial z|$ with a correlation coefficient of 0.52 (statistically significant at the 95% significance level). This provides further evidence on the dominant contribution of Ekman flow to the vertical shear and associated kinetic energy transfer to submesoscale eddies. Finally, it should be noted that this energy transfer should be distinguished from the energy transfer through the turbulent thermal wind and down-front wind mechanisms (Thomas and Lee 2005; Thomas et al. 2008; Gula et al. 2014; McWilliams et al. 2015). In those mechanisms, the presence of strong density gradient is essential, and the energy transfer is achieved through an upward buoyancy flux of submesoscale eddies. However, the energy transfer here is achieved through the MKE_6 term, and the density gradient does not play an important role. In fact, the value of $|\partial\overline{v}_a/\partial z|$ derived from the frontal Ekman equation is similar to that derived from the standard Ekman equation (Figs. 13d,e).

In June–September (the growing phase of SMKE), the intertropical convergence zone migrates northward and the trade winds accelerate the SEC (Vialard et al. 2003). This intensifies the horizontal shear between SEC and NECC, favoring the generation of TIWs (Philander 1978). The latter further enhances the horizontal strain rate in their northern edge and contributes to the increased MKE term during this season. Furthermore, the trade wind stress also becomes stronger during August–September (Talley 2011), which enhances the vertical ageostrophic shear to further increase MKE production.

5. Conclusions

In this study, the spatial and seasonal variations of submesoscale eddy activity in the east equatorial Pacific

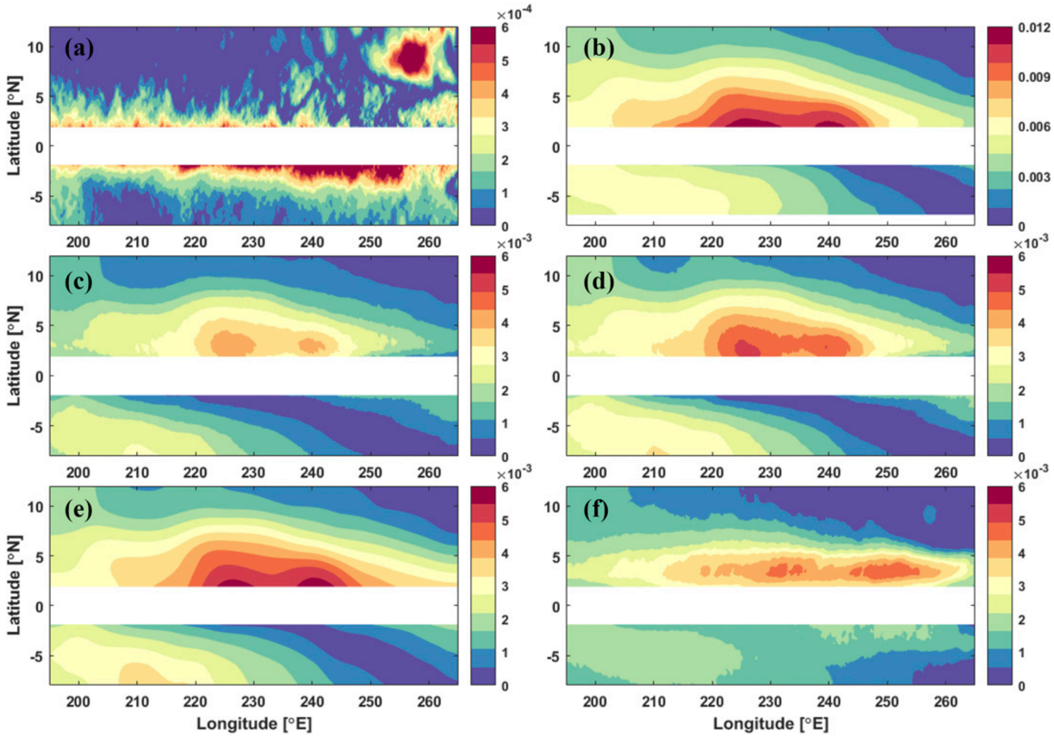

FIG. 13. (a) The magnitude of time-mean $|\partial \overline{v}_g/\partial z|$ in the mixed layer. The magnitude of time-mean $|\partial \overline{v}_a/\partial z|$ calculated from frontal Ekman equation with viscosity (b) 1×10^{-3}, (c) 1×10^{-2}, and (d) $8 \times 10^{-3}\, m^2\, s^{-1}$. (e) As in (d), but calculated from classical Ekman equation. (f) The magnitude of time-mean $|\partial \overline{v}/\partial z|$ calculated from the meridional velocity from LICOM.

Ocean (2°–12°N, 95°–165°W) are investigated based on a 1/10° OGCM. The major conclusions are summarized as follows:

1) In the studied region, flows with horizontal scales shorter than 500 km are subject to submesoscale dynamics with an $O(1)$ Rossby number and a -2 spectral slope for kinetic energy. It suggests that the horizontal scale of submesoscale eddies in the equatorial region is more than an order of magnitude larger than that at midlatitudes so that they can be well resolved by a 1/10° OGCM.
2) SMKE exhibits pronounced spatial variability. Energetic submesoscale eddies reside in the surface mixed layer around the northern edge (5°N) of TIWs. A complete SMKE budget analysis suggests that the barotropic and baroclinic energy conversions account for about 78% and 14% of the energy source in the mixed layer, respectively. The strong barotropic energy conversion occurs mainly through the horizontal strain because of TIWs and vertical shear caused by the wind-induced Ekman flow. The nonlinear interactions lead to a significant forward energy cascade and are important in balancing the energy budget.
3) There are pronounced seasonal variations in the mixed layer SMKE with the largest and smallest values occurring in August–October and March–May, respectively. The seasonal cycle of SMKE is mainly attributed to the seasonal change of energy input through barotropic instability and to a less extent baroclinic instability.
4) The restratification effect induced by submesoscale eddies is comparable to that by TIWs. In particular, both effects are strongest during July–October. This leads to significant reduction of MLD during July–October, although the atmospheric forcing favors the deepening of MLD in this period.

The results in this study reveal the pronounced difference in the submesoscale eddy dynamics between the midlatitudes and the equatorial region. Unlike the midlatitudes, it is the barotropic instability rather than the baroclinic instability that contributes dominantly to the generation of submesoscale eddies in the equatorial east Pacific. The seasonal cycle of SMKE in the equatorial east Pacific is mainly modulated by the seasonal variation of horizontal strain rate and vertical shear of background flows. As a result, its seasonal cycle does not necessarily follow that of MLD as at the midlatitudes. Indeed, the

SMKE in the equatorial east Pacific peaks in September, whereas the MLD reaches its maximum in July–August.

As demonstrated in this study, the submesoscale eddies contribute significantly to the restratification process in the eastern tropical Pacific Ocean and thus play an important role in the mixed layer heat budget. Although the horizontal scale of equatorial submesoscale eddies is much larger than their counterpart at the midlatitudes, they are still poorly represented in the current generation of climate models with a typical horizontal grid size of 1°. This might lead to significant biases in the simulated SST and MLD in the eastern tropical Pacific Ocean, which could further affect the entire equatorial circulation through the strong air–sea coupling there (Imada and Kimoto 2012). Therefore, high-resolution climate models with equatorial submesoscale eddies well resolved are necessary to reduce internal uncertainties in prediction and projection of future ocean climate changes.

Acknowledgments. This research is supported by National Natural Science Foundation of China (NSFC) (U1606402, 41521091, and 41490643), Qingdao National Laboratory for Marine Science and Technology (2015ASKJ01 and 2017ASTCP-ES05), and China National Global Change Major Research Project (2013CB956201).

REFERENCES

Arbic, B. K., K. L. Polzin, R. B. Scott, J. G. Richman, and J. F. Shriver, 2013: On eddy viscosity, energy cascades, and the horizontal resolution of gridded satellite altimeter products. *J. Phys. Oceanogr.*, **43**, 283–300, https://doi.org/10.1175/JPO-D-11-0240.1.

Barkan, R., K. B. Winters, and S. G. Llewellyn Smith, 2015: Energy cascades and loss of balance in a reentrant channel forced by wind stress and buoyancy fluxes. *J. Phys. Oceanogr.*, **45**, 272–293, https://doi.org/10.1175/JPO-D-14-0068.1.

Baturin, N., and P. Niiler, 1997: Effects of instability waves in the mixed layer of the equatorial Pacific. *J. Geophys. Res.*, **102**, 27 771–27 793, https://doi.org/10.1029/97JC02455.

Boccaletti, G., R. Ferrari, and B. Fox-Kemper, 2007: Mixed layer instabilities and restratification. *J. Phys. Oceanogr.*, **37**, 2228–2250, https://doi.org/10.1175/JPO3101.1.

Brannigan, L., D. P. Marshall, A. Naveira-Garabato, and A. G. Nurser, 2015: The seasonal cycle of submesoscale flows. *Ocean Modell.*, **92**, 69–84, https://doi.org/10.1016/j.ocemod.2015.05.002.

Brüggemann, N., and C. Eden, 2015: Routes to dissipation under different dynamical conditions. *J. Phys. Oceanogr.*, **45**, 2149–2168, https://doi.org/10.1175/JPO-D-14-0205.1.

Callies, J., R. Ferrari, J. M. Klymak, and J. Gula, 2015: Seasonality in submesoscale turbulence. *Nat. Commun.*, **6**, 6862, https://doi.org/10.1038/ncomms7862.

Canuto, V. M., A. Howard, Y. Cheng, and M. S. Dubovikov, 2001: Ocean turbulence. Part I: One-point closure model-momentum and heat vertical diffusivities. *J. Phys. Oceanogr.*, **31**, 1413–1426, https://doi.org/10.1175/1520-0485(2001)031<1413:OTPIOP>2.0.CO;2.

——, ——, ——, and ——, 2002: Ocean turbulence. Part II: Vertical diffusivities of momentum, heat, salt, mass, and passive scalars. *J. Phys. Oceanogr.*, **32**, 240–264, https://doi.org/10.1175/1520-0485(2002)032<0240:OTPIVD>2.0.CO;2.

Capet, X., E. Campos, and A. Paiva, 2008a: Submesoscale activity over the Argentinian shelf. *Geophys. Res. Lett.*, **35**, L15605, https://doi.org/10.1029/2008GL034736.

——, J. C. McWilliams, M. J. Molemaker, and A. Shchepetkin, 2008b: Mesoscale to submesoscale transition in the California Current System. Part I: Flow structure, eddy flux, and observational tests. *J. Phys. Oceanogr.*, **38**, 29–43, https://doi.org/10.1175/2007JPO3671.1.

——, ——, ——, and ——, 2008c: Mesoscale to submesoscale transition in the California Current System. Part II: Frontal processes. *J. Phys. Oceanogr.*, **38**, 44–64, https://doi.org/10.1175/2007JPO3672.1.

——, ——, ——, and ——, 2008d: Mesoscale to submesoscale transition in the California Current System. Part III: Energy balance and flux. *J. Phys. Oceanogr.*, **38**, 2256–2269, https://doi.org/10.1175/2008JPO3810.1.

Charney, J. G., 1971: Geostrophic turbulence. *J. Atmos. Sci.*, **28**, 1087–1095, https://doi.org/10.1175/1520-0469(1971)028<1087:GT>2.0.CO;2.

Couvelard, X., F. Dumas, V. Garnier, A. L. Ponte, C. Talandier, and A. M. Treguier, 2015: Mixed layer formation and restratification in presence of mesoscale and submesoscale turbulence. *Ocean Modell.*, **96**, 243–253, https://doi.org/10.1016/j.ocemod.2015.10.004.

Cravatte, S., and C. Menkes, 2009: Sensitivity of mixed layer heat budgets to wind forcing: A case study for the equatorial Pacific cold tongue. *Ocean Modell.*, **29**, 198–212, https://doi.org/10.1016/j.ocemod.2009.04.005.

Cronin, M. F., and W. S. Kessler, 2009: Near-surface shear flow in the tropical Pacific cold tongue front. *J. Phys. Oceanogr.*, **39**, 1200–1215, https://doi.org/10.1175/2008JPO4064.1.

Eady, E. T., 1949: Long waves and cyclone waves. *Tellus*, **1** (3), 33–52, https://doi.org/10.3402/tellusa.v1i3.8507.

Fox-Kemper, B., and R. Ferrari, 2008: Parameterization of mixed layer eddies. Part II: Prognosis and impact. *J. Phys. Oceanogr.*, **38**, 1166–1179, https://doi.org/10.1175/2007JPO3788.1.

——, ——, and R. Hallberg, 2008: Parameterization of mixed layer eddies. Part I: Theory and diagnosis. *J. Phys. Oceanogr.*, **38**, 1145–1165, https://doi.org/10.1175/2007JPO3792.1.

Gibson, J. K., P. Kållberg, S. Uppala, A. Hernandez, A. Nomura, and E. Serrano, 1999: ECMWF Re-Analysis project report series: 1. ERA-15 description. ECMWF Rep., 84 pp.

Graham, T., 2014: The importance of eddy permitting model resolution for simulation of the heat budget of tropical instability waves. *Ocean Modell.*, **79**, 21–32, https://doi.org/10.1016/j.ocemod.2014.04.005.

Gula, J., M. J. Molemaker, and J. C. McWilliams, 2014: Submesoscale cold filaments in the Gulf Stream. *J. Phys. Oceanogr.*, **44**, 2617–2643, https://doi.org/10.1175/JPO-D-14-0029.1.

Haney, S., and Coauthors, 2012: Hurricane wake restratification rates of one-, two- and three-dimensional processes. *J. Mar. Res.*, **70**, 824–850, https://doi.org/10.1357/002224012806770937.

Holmes, R., and L. Thomas, 2016: Modulation of tropical instability wave intensity by equatorial Kelvin waves. *J. Phys. Oceanogr.*, **46**, 2623–2643, https://doi.org/10.1175/JPO-D-16-0064.1.

Huang, Z., P. Lin, and H. U. Jianyu, 2017: Influence of island chains on the Kuroshio intrusion in the Luzon Strait. *Adv. Atmos. Sci.*, **34**, 397–410, https://doi.org/10.1007/s00376-016-6159-y.

Imada, Y., and M. Kimoto, 2012: Parameterization of tropical instability waves and examination of their impact on ENSO characteristics. *J. Climate*, **25**, 4568–4581, https://doi.org/10.1175/JCLI-D-11-00233.1.

Kara, A. B., P. A. Rochford, and H. E. Hurlburt, 2003: Mixed layer depth variability over the global ocean. *J. Geophys. Res.*, **108**, 3079, https://doi.org/10.1029/2000JC000736.

Kennan, S. C., and P. J. Flament, 2000: Observations of a tropical instability vortex. *J. Phys. Oceanogr.*, **30**, 2277–2301, https://doi.org/10.1175/1520-0485(2000)030<2277:OOATIV>2.0.CO;2.

Klein, P., B. L. Hua, G. Lapeyre, X. Capet, S. Le Gentil, and H. Sasaki, 2008: Upper ocean turbulence from high-resolution 3D simulations. *J. Phys. Oceanogr.*, **38**, 1748–1763, https://doi.org/10.1175/2007JPO3773.1.

——, G. Lapeyre, G. Roullet, S. L. Gentil, and H. Sasaki, 2011: Ocean turbulence at meso and submesoscales: Connection between surface and interior dynamics. *Geophys. Astrophys. Fluid Dyn.*, **105**, 421–437, https://doi.org/10.1080/03091929.2010.532498.

Large, W. G., and S. G. Yeager, 2004: Diurnal to decadal global forcing for ocean and sea-ice models: The data sets and flux climatologies. NCAR Tech. Note NCAR/TN-460+STR, 105 pp., https://doi.org/10.5065/D6KK98Q6.

Lévy, M., P. Klein, and A. M. Treguier, 2001: Impact of submesoscale physics on production and subduction of phytoplankton in an oligotrophic regime. *J. Mar. Res.*, **59**, 535–565, https://doi.org/10.1357/002224001762842181.

——, ——, ——, D. Iovino, G. Madec, S. Masson, and K. Takahashi, 2010: Modifications of gyre circulation by submesoscale physics. *Ocean Modell.*, **34**, 1–15, https://doi.org/10.1016/j.ocemod.2010.04.001.

——, R. Ferrari, P. J. S. Franks, A. P. Martin, and P. Rivière, 2012: Bringing physics to life at the submesoscale. *Geophys. Res. Lett.*, **39**, L14602, https://doi.org/10.1029/2012GL052756.

Liu, H., Y. Yu, P. Lin, and F. Wang, 2014: High-resolution LICOM. *Flexible Global Ocean-Atmosphere-Land System Model: A Modeling Tool for the Climate Change Research Community*, T. Zhou et al., Eds., Springer, 321–331.

Lyman, J. M., G. C. Johnson, and W. S. Kessler, 2007: Distinct 17- and 33-day tropical instability waves in subsurface observations. *J. Phys. Oceanogr.*, **37**, 855–872, https://doi.org/10.1175/JPO3023.1.

Mahadevan, A., and D. Archer, 2000: Modeling the impact of fronts and mesoscale circulation on the nutrient supply and biogeochemistry of the upper ocean. *J. Geophys. Res.*, **105**, 1209–1225, https://doi.org/10.1029/1999JC900216.

Marchesiello, P., X. Capet, C. Menkes, and S. C. Kennan, 2011: Submesoscale dynamics in tropical instability waves. *Ocean Modell.*, **39**, 31–46, https://doi.org/10.1016/j.ocemod.2011.04.011.

McWilliams, J. C., 2016: Submesoscale currents in the ocean. *Proc. Roy. Soc.*, **A472**, 20160117, https://doi.org/10.1098/rspa.2016.0117.

——, J. Gula, M. J. Molemaker, L. Renault, and A. F. Shchepetkin, 2015: Filament frontogenesis by boundary layer turbulence. *J. Phys. Oceanogr.*, **45**, 1988–2005, https://doi.org/10.1175/JPO-D-14-0211.1.

Menkes, C. E., J. G. Vialard, S. C. Kennan, J.-P. Boulanger, and G. V. Madec, 2006: A modeling study of the impact of tropical instability waves on the heat budget of the eastern equatorial Pacific. *J. Phys. Oceanogr.*, **36**, 847–865, https://doi.org/10.1175/JPO2904.1.

Mensa, J. A., Z. Garraffo, A. Griffa, T. M. Özgökmen, A. Haza, and M. Veneziani, 2013: Seasonality of the submesoscale dynamics in the Gulf Stream region. *Ocean Dyn.*, **63**, 923–941, https://doi.org/10.1007/s10236-013-0633-1.

Molemaker, M. J., J. C. McWilliams, and X. Capet, 2010: Balanced and unbalanced routes to dissipation in an equilibrated Eady flow. *J. Fluid Mech.*, **654**, 35–63, https://doi.org/10.1017/S0022112009993272.

Munk, W., L. Armi, K. Fischer, and F. Zachariasen, 2000: Spirals on the sea. *Proc. Roy. Soc. London*, **456A**, 1217–1280, https://doi.org/10.1098/rspa.2000.0560.

Ni, R., G. A. Voth, and N. T. Ouellette, 2014: Extracting turbulent spectral transfer from under-resolved velocity fields. *Phys. Fluids*, **26**, 105107, https://doi.org/10.1063/1.4898866.

Nurser, A. J. G., and J. W. Zhang, 2000: Eddy-induced mixed layer shallowing and mixed layer/thermocline exchange. *J. Geophys. Res.*, **105**, 21 851–21 868, https://doi.org/10.1029/2000JC900018.

Philander, S. G. H., 1978: Instabilities of zonal equatorial currents. *J. Geophys. Res.*, **83**, 3679–3682, https://doi.org/10.1029/JC083iC07p03679.

Ponte, A. L., P. Klein, X. Capet, P. Y. L. Traon, B. Chapron, and P. Lherminier, 2013: Diagnosing surface mixed layer dynamics from high-resolution satellite observations: Numerical insights. *J. Phys. Oceanogr.*, **43**, 1345–1355, https://doi.org/10.1175/JPO-D-12-0136.1.

Qiu, B., T. Nakano, S. Chen, and P. Klein, 2017: Submesoscale transition from geostrophic flows to internal waves in the northwestern Pacific upper ocean. *Nat. Commun.*, **8**, 14055, https://doi.org/10.1038/ncomms14055.

Roske, F., 2001: An atlas of surface fluxes based on the ECMWF Re-Analysis? A climatological dataset to force global ocean general circulation models. Max-Planck Institut fur Meteorologie Rep. 323, 41 pp.

Rosso, I., A. M. Hogg, P. G. Strutton, A. E. Kiss, R. Matear, A. Klocker, and E. V. Sebille, 2014: Vertical transport in the ocean due to sub-mesoscale structures: Impacts in the Kerguelen region. *Ocean Modell.*, **80**, 10–23, https://doi.org/10.1016/j.ocemod.2014.05.001.

Santiago-Mandujano, F., and E. Firing, 1990: Mixed-layer shear generated by wind stress in the central equatorial Pacific. *J. Phys. Oceanogr.*, **20**, 1576–1582, https://doi.org/10.1175/1520-0485(1990)020<1576:MLSGBW>2.0.CO;2.

Sasaki, H., P. Klein, B. Qiu, and Y. Sasai, 2014: Impact of oceanic-scale interactions on the seasonal modulation of ocean dynamics by the atmosphere. *Nat. Commun.*, **5**, 5636, https://doi.org/10.1038/ncomms6636.

Schlösser, F., and C. Eden, 2007: Diagnosing the energy cascade in a model of the North Atlantic. *Geophys. Res. Lett.*, **34**, L02604, https://doi.org/10.1029/2006GL027813.

Scott, R. B., and F. Wang, 2005: Direct evidence of an oceanic inverse kinetic energy cascade from satellite altimetry. *J. Phys. Oceanogr.*, **35**, 1650–1666, https://doi.org/10.1175/JPO2771.1.

Scully-Power, P., 1986: Navy oceanographer shuttle observations: STS 41-G mission report. Navy Space Oceanography Committee Rep., 146 pp.

Talley, L. D., 2011: *Descriptive Physical Oceanography: An Introduction.* 6th ed. Academic Press, 560 pp.

Thomas, L. N., and C. M. Lee, 2005: Intensification of ocean fronts by down-front winds. *J. Phys. Oceanogr.*, **35**, 1086–1102, https://doi.org/10.1175/JPO2737.1.

——, A. Tandon, and A. Mahadevan, 2008: Submesoscale processes and dynamics. *Ocean Modeling in an Eddying Regime*, *Geophys. Monogr.*, Vol. 177, Amer. Geophys. Union, 17–38.

Vialard, J., C. Menkes, D. L. Anderson, and M. A. Balmaseda, 2003: Sensitivity of Pacific Ocean tropical instability waves to initial conditions. *J. Phys. Oceanogr.*, **33**, 105–121, https://doi.org/10.1175/1520-0485(2003)033<0105:SOPOTI>2.0.CO;2.

Yu, Y., H. Liu, and P. Lin, 2012: A quasi-global 1/10° eddy-resolving ocean general circulation model and its preliminary results. *Sci. Bull.*, **57**, 3908–3916, https://doi.org/10.1007/s11434-012-5234-8.